IET Journals
The Institution of Engineering and Technology

Two-dimensional autofocus technique for high-resolution spotlight synthetic aperture radar

Le-tian Zeng[1], Yi Liang[1,2] ✉, Meng-dao Xing[1,2], Zhen-yu Li[1], Yuan-yuan Huai[1]

[1]*National Laboratory of Radar Signal Processing, Xidian University, Xi'an 710071, People's Republic of China*
[2]*Collaborative Innovation Center of Information Sensing and Understanding at Xidian University, Xi'an 710071, People's Republic of China*
✉ *E-mail: yliang@xidian.edu.cn*

Abstract: Motion errors are inevitably introduced when data is acquired and considerably degrade the image quality in terms of geometric resolution, radiometric accuracy and image contrast, especially in high-resolution spotlight synthetic aperture radar (SAR) imagery. In this study, the authors present a novel two-dimensional (2D) autofocus algorithm directly inserted into polar format algorithm, which compensates the envelop error and the phase error sequentially. A coarse error correction is first performed by global positioning system or inertial navigation system in the range-compressed domain, then a new envelop compensation strategy, stage-by-stage approach, is designed, obtaining promising results for removing range cell migration after 2D interpolation. Additionally, a weighed contrast enhancement autofocus algorithm based on spatially variant model is developed to compensate for the residual phase error, which remarkably improves the estimation accuracy. The presented algorithm is very robust to deal with substantial errors over a variety of scenes even in conditions of homogenous areas with no prominent point scatterers and enables the utilisation of fast Fourier transform. The experimental results obtained by the proposed algorithm confirm that the analysis extends well to realistic situations.

1 Introduction

The irregular motion of the synthetic aperture radar (SAR) platform caused by atmosphere turbulence as well as its own vibration yields substantial envelop migrations into other range cells and complicated phase aberrations, which considerably degrades SAR focus [1–3]. Such errors can be partly cancelled by a navigation system, but for very high-resolution data, broadening of the SAR impulse response function deteriorates the resolution, and autofocus algorithms must be developed to estimate residual errors beyond the capacity of the navigation system.

There are a number of data-driven autofocus techniques that attempt to correct motion errors [4, 5]. The conventional map-drift (MD) autofocus algorithm [6] is to model the motion error as a second-order polynomial and estimates the Doppler rate of the radar echoes to calculate the corresponding acceleration, but it is inadequate in high-resolution SAR imaging with a long synthetic aperture as well as an unpredictable trajectory. As the industry standard, phase gradient autofocus (PGA) algorithm [7–9] is a non-parameterised method which computes the first derivative of the phase error based on the information about isolated point scatterers. However, poor results are obtained when it comes to the content with homogeneous areas in the image, such as desert, grassland and sea surface. A more recent class encompasses algorithms that determine the phase error estimation which minimises or maximises a particular cost function [10–12] and correct the blurred images. Nevertheless, this image restoration technique is usually computationally intensive and usually liable to be influenced by its specific iterative strategy in certain circumstances.

In this paper, we propose a novel two-dimensional (2D) autofocus scheme combined with polar format algorithm (PFA) [1] for high-resolution spotlight SAR imaging. First of all, navigation information read by global positioning system or inertial navigation system (GPS/INS) onboard the airplane is employed to perform the coarse compensation of the range-compressed data,

which is composed of partial range cell migration correction (RCMC) and preliminary phase error cancellation. Then, beginning with the polar formatted phase history data, a new RCMC strategy is developed that estimates the migration and performs envelop and phase corrections to account for the residual motion errors. Additionally, a weighted contrast enhancement autofocus (WCEA) algorithm based on spatially variant model is utilised to correct the residual phase error, acquiring good results with modest processing. By means of image metric of contrast which is inherently independent of the image content and does not need bright targets, this scheme has the ability to compensate motion errors to a very accurate degree, and apparently, is more suitable for homogenous areas in real-world SAR imaging. A battery of real data experiments is used to validate the excellent capability of the new algorithm compared with existing algorithms.

2 Signal model and motion error model

The spotlight SAR data acquisition geometry is shown in Fig. 1, where the radar antenna is continually steered onto the scene centre T_0. Assuming that the imaged area is flat, we construct a Cartesian coordinate system O-XYZ on the ground. The dashed line with points S, Q and E on it, called the nominal trajectory, is parallel to the X-axis while the solid line represents the real trajectory. In ideal case, the antenna phase centre (APC) P of the radar moves at a constant velocity v_0 along the nominal path on the synthetic aperture (from S to E). Also, P satisfies the conditions $PG \perp OGT_0$, $SE \perp PGT_2$, $|PG| = H$ and $|PT_2| = R_s$, where G and T_2 are the projections of P on the ground and a certain target located on the centre-line of the imaged scene, respectively. However, some unpredictable errors in practice induce the platform deviating from the ideal trajectory and travelling along a curved line. Herein, we restrict our discussion to the case where the 'stop-go' approximation holds and the SAR platform works in the broadside mode. Also, we define the plane rectangular
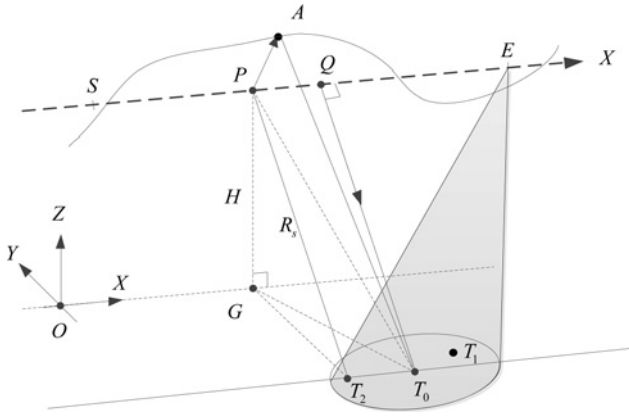
Fig. 1 *Spotlight SAR data acquisition geometry*

coordinate system XQT_0 on the slant plane as the imaging coordinate system and consider the moment when the APC flies over Q, the centre of the synthetic aperture with $EQ \perp QT_0$ and $|QT_0| = R_s$, as the zero point of azimuth time t_a. Thus, the ideal position P and actual position A of the APC at t_a are $(v_0 t_a, 0)$ and $(v_0 t_a + \Delta x(t_a),$ $\Delta r_1(t_a))$, separately, where $\Delta x(t_a)$ is the along-track error and $\Delta r_1(t_a)$ is the cross-track error. For an arbitrary point target $T_1(x,$ $R_s + r)$ on the slant plane, the ideal and actual instantaneous range from APC to it can be written as

$$R_0(t_a; x, r) = \sqrt{(v_0 t_a - x)^2 + (R_s + r)^2} \tag{1}$$

$$R(t_a; x, r) = \sqrt{(v_0 t_a + \Delta x(t_a) - x)^2 + (\Delta r_1(t_a) - R_s - r)^2} \tag{2}$$

$$R(t_a; x, r) = R_0(t_a; x, r) + \Delta R(t_a; x, r) \tag{3}$$

where $\Delta R(t_a; x, r)$ represents the range error caused by motion errors. Thus, the demodulated echo from T_1 can be formulated as

$$ss(\tau, t_a; x, r) = \text{rect}\left[\frac{(\tau - 2(R(t_a; x, r)/c))}{T_p}\right]$$
$$\times \exp\left[j\pi\gamma\left(\tau - 2\frac{R(t_a; x, r)}{c}\right)^2\right]$$
$$\times \exp\left[-j\frac{4\pi f_c}{c}R(t_a; x, r)\right] \tag{4}$$

where τ is the fast time; T_p is the pulse width

$$\text{rect}(\tau) = \begin{cases} 1, & |\tau| \leq \frac{1}{2} \\ 0, & \text{else} \end{cases}$$

and γ signifies the chirp rate; f_c denotes the carrier frequency and c defines the propagation velocity of the echo.

After range compression is implemented, we have

$$ss(\tau, t_a; x, r) = \text{rect}\left[\frac{(\tau - 2(R(t_a; x, r)/c))}{T_p}\right]$$
$$\times \exp\left[-j\frac{4\pi}{\lambda}R_0(t_a; x, r)\right]$$
$$\times \exp[j\varphi(t_a; x, r)] \tag{5}$$

where $\lambda = c/f_c$ is the wavelength; $\varphi(t_a; x, r) = -(4\pi/\lambda)\Delta R(t_a; x, r)$ describes the phase error introduced by the unpredictable motion of the platform and satisfies the condition $\varphi(t_a; x, r) = \varphi_{\text{err}}(t_a) + \varphi_{\text{err1}}(t_a; x, r)$, which is composed of two parts: one is

range-invariant component $\varphi_{\text{err}}(t_a)$ and the other is spatially variant component $\varphi_{\text{err1}}(t_a; x, r)$. Here, we can exploit the navigation information to determine the along-track velocity error and the cross-track range error. By calculating the cross-track error, coarse corrections of the envelop error and the corresponding phase error are applied. Then the phase error caused by the along-track velocity error is found via the double integration of the Doppler rate in the processing time.

Assume that $v_r(t_a)$ is the radical velocity along the line of sight, which can be read by the GPS/INS, then we can obtain the instantaneous slant range error $\Delta r(t_a)$, which yields

$$\Delta r(t_a) = \int_0^{t_a} v_r(\zeta)d\zeta + \Delta r(0) \tag{6}$$

where $\Delta r(0)$ denotes the opposite number of the mean of $\int_0^{t_a} v_r(\zeta)d\zeta$. Therefore, the envelop error in (6) can be corrected in the range frequency domain and the phase error can be accounted for by the following equation in the fast time domain

$$\phi_r(t_a) = -\frac{4\pi}{\lambda}\Delta r(t_a) \tag{7}$$

Supposing that the forward velocity of the platform in T_a is $v_x(t_a)$ ($t_a \in [0, T_a]$ and T_a is the processing time of the data), we denote $v_1 = \int_0^{T_a} v_x(\zeta)d\zeta/T_a$ as the mean of $v_x(t_a)$ ($t_a \in [0, T_a]$). The associated Doppler rate can be written as

$$K_a(t_a) = -\frac{2v_x^2(t_a)}{\lambda R_s}, \quad t_a \in [0, T_a] \tag{8}$$

The deviations of $v_x(t_a)$ from v_1 lead to the variations of the Doppler rate, which yields

$$\Delta K_a(t_a) = -\frac{2v_x^2(t_a)}{\lambda R_s} + \frac{2v_1^2}{\lambda R_s}, \quad t_a \in [0, T_a] \tag{9}$$

Hence, the along-track phase error can be compensated by the following expression

$$\phi_a(t_a) = 2\pi \int_0^{t_a}\int_0^{s_a} \Delta K_a(\zeta)d\zeta ds_a, \quad 0 \leq t_a, \quad s_a \leq T_a \tag{10}$$

According to the flow of PFA, applying fast Fourier transform (FFT) with respect to τ in (5) and subsequently carrying out azimuth dechirp (multiplying by $\exp\left[j(4\pi/c)(f_c + f_r)\sqrt{(v_0 t_a)^2 + R_s^2}\right]$), we have

$$Ss(k_r, t_a; x, r) = \text{rect}\left[\frac{k_r - k_0}{4\pi B/c}\right] \times \exp\left[-jk_r\frac{R_s}{\sqrt{(v_0 t_a)^2 + R_s^2}}r\right]$$
$$\times \exp\left[jk_r\frac{v_0 t_a}{\sqrt{(v_0 t_a)^2 + R_s^2}}x\right]$$
$$\times \exp[-jk_r\Delta R_{\text{res}}(t_a; x, r)] \tag{11}$$

where $B = \gamma T_p$ is the signal bandwidth; f_r indicates the range frequency; $k_r = (4\pi/c)(f_c + f_r)$ and $k_0 = (4\pi/c)f_c$ denote the range wavenumber and its centre, respectively; $\Delta R_{\text{res}}(t_a; x, r)$ signifies the residual range error after being roughly accounted for by the GPS/INS.

By substituting $k_y = k_r\left(R_s/\sqrt{(v_0 t_a)^2 + R_s^2}\right)$ and $k_x = k_r\left(v_0 t_a/\sqrt{(v_0 t_a)^2 + R_s^2}\right)$ into (11) which is also called 2D

interpolation, we obtain the expression as

$$SS\left(k_x, k_y; x, r\right) \simeq \text{rect}\left[\frac{k_y - k_0}{4\pi B/c}\right] \times \exp\left(-jk_y r\right) \times \exp\left(jk_x x\right)$$
$$\times \exp\left[-j\psi\left(\frac{k_x R_s}{k_y v_0}; x, r\right)\right] \quad (12)$$

where $\psi\left(\left(k_x/k_y\right)\left(R_s/v_0\right); x, r\right) = \sqrt{k_x^2 + k_y^2} \times \Delta R_{\text{res}}\left(\left(k_x/k_y\right)\left(R_s/v_0\right); x, r\right)$ represents the residual phase error with the impact of the resampling operation and can be consisted of the spatially invariant component $\psi_{\text{err}}((k_x/k_y)(R_s/v_0))$ and the spatially variant component $\psi_{\text{err1}}((k_x/k_y)(R_s/v_0); x, r)$. That is, the PFA resampling has introduced a (k_x/k_y) dependency in the phase error term that changes the shape of the envelope compared with that of the envelope before 2D interpolation [13, 14], leading to an additional shifting beyond the range resolution cell during the course of the synthetic aperture. Also, it can be highly non-linear and varies essentially with the positions of the targets. Hence, our aim is to present a novel autofocus algorithm to correct the envelope error as well as the phase error, overcoming the impacts of PFA on the residual envelope error of the signal to the maximum degree.

3 Excessive residual envelope error correction

While the presumption of the range error being less than the radar's range resolution is often true, high-resolution SARs do sometimes exceed this criterion in the situations where a target's echo effectively exhibits a residual range cell migration (RCM) error exceeding one or more range resolution cells during the course of the synthetic aperture. This would doom to failure any autofocus scheme that presupposes. In this section, an approximate expression of the envelope error after 2D interpolation is derived and a new envelop compensation strategy is designed to remove the RCM.

3.1 Derivation of the excessive range migration

To facilitate the analysis of the excessive range migration, a Taylor expansion of the phase error $\psi_{\text{err}}((k_x/k_y)(R_s/v_0))$ with respect to $k_y = k_0$ is performed without considering the impacts of $\psi_{\text{err1}}((k_x/k_y)(R_s/v_0); x, r)$ on RCM, which yields

$$\psi_{\text{err}}\left(\frac{k_x R_s}{k_y v_0}\right) = \psi_0 + \psi_1 \times \left(k_y - k_0\right) + \cdots \quad (13)$$

where the first term in the right hand is the phase error term, and the

second term is related to the excessive RCM, which results from the effects of the polar formatting on the residual envelope error. The influences of the higher order terms on the envelope error, in general, are not significant and ignored here. By a simplistic calculation, the first two coefficients in (13) can be derived as

$$\psi_0 = \sqrt{k_x^2 + k_0^2} \times \Delta R_{\text{res}}\left(\frac{k_x R_s}{k_0 v_0}\right) \quad (14)$$

$$\psi_1 = \frac{k_0}{\sqrt{k_x^2 + k_0^2}} \times \Delta R_{\text{res}}\left(\frac{k_x R_s}{k_0 v_0}\right) - \frac{k_x\sqrt{k_x^2 + k_0^2}}{k_0^2} \times \frac{R_s}{v_0}$$
$$\times \Delta R'_{\text{res}}\left(\frac{k_x R_s}{k_0 v_0}\right) \quad (15)$$

where $\Delta R'_{\text{res}}((k_x/k_0)(R_s/v_0)) = (d/dx)(\Delta R_{\text{res}}(x))|_{x=(k_x/k_0)(R_s/v_0)}$ signifies the effects of polar formatting on the residual envelope error and apparently, the linear relationship between the envelope error and the phase error does not hold anymore. After range inverse FFT of $\Delta k_y = k_y - k_0$ in (12) and ignoring the constant phase terms, we have

$$sS\left(\tau, k_x; x, r\right) \simeq \text{rect}\left[\frac{(\tau - 2(r + \psi_1/c))}{T_p}\right] \times \exp\left(jk_x x\right)$$
$$\times \exp\left(-j\psi_0\right) \quad (16)$$

If ψ_1 were not properly corrected, the migration would surpass one range cell in the range-compressed domain. To estimate ψ_0, we should perform under-sampling of the range-compressed data along the range dimension to capture the variation of the envelope into a coarse range cell. An effective way is to sum up some neighbouring range cells into a single range cell [5]. Once done, an accurate estimate of the spatially invariant phase error ψ_0 can be retrieved by weighted least-square PGA (WPGA) [15] and the envelope error can also be achieved and corrected.

For clarity, we design a numerical example to explain the effect of polar formatting on residual envelope error. Taking $R_s = 6$ km, $v_0 = 80$ m/s and the platform flying from -256 to 256 m in the azimuth direction, the residual envelope error is assumed as a sine function shown in Fig. 2a, and the corresponding RCM error after 2D interpolation is given in Fig. 2b. In Fig. 2a, we note that the envelop error varies within only several centimetres, which is beyond the capacity of the navigation system. However, the corresponding RCM is magnified up to several times and substantially changes its shape after the polar formatting, which surely exceeds one resolution cell in high-resolution SAR. In other words, even very small residual envelope error is left after coarse motion compensation (MOCO), serious RCM presents after 2D interpolation. Hence, we should apply WPGA algorithm to the down-sampling data to determine the variation of the envelope.
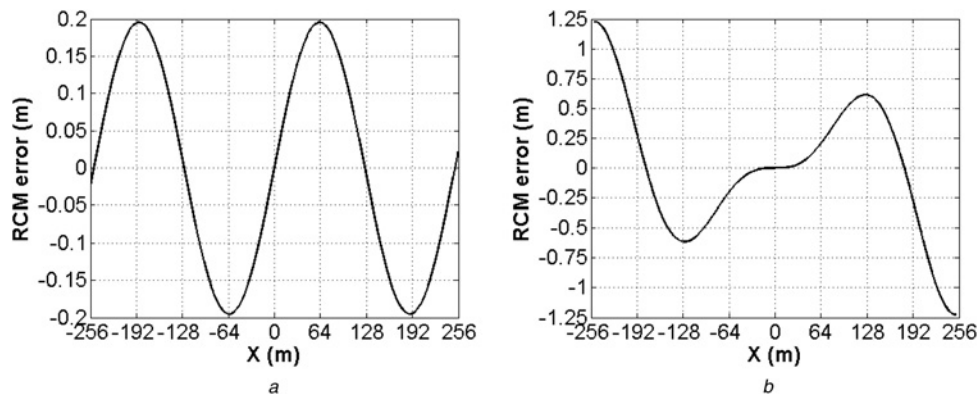

Fig. 2 *Residual envelop error*
a Before 2D interpolation
b After 2D interpolation

3.2 Implementation of excessive RCM correction

For robust correction, we adopt a stage-by-stage approach (SSA) by decreasing the number of neighbouring range cells in each under-sampling iteration, which is implemented by summing up L neighbouring range bins into a single range bin to include the excessive RCM in it. In the initial several iterations, L is set to be large (ten for instance) because of the serious range migration. WPGA is adopted to calculate the phase error with the under-sampling data. Then a low-order (four for instance) polynomial fitting is utilised to calculate the coarse phase error and subsequently remove both the envelop error and the phase error, with smaller range migration left in the data. In the following iterations, L decreases by a factor of two and correspondingly, higher order polynomial fitting is employed to get finer estimation of both the residual envelop error and phase error. The whole procedure is repeated until the proper value of the envelop error is obtained – SSA stops when the envelop error is smaller than 1/4 the original range resolution cell. In practice, the algorithm stops after three to five iterations. At the final stage of the algorithm, the estimated envelop error is used for the envelop correction and phase compensation, and a straight envelop line within a single range resolution cell is obtained.

However, we must make it clear that the accuracies of correcting the envelop error and removing the phase error are considerably different in SAR MOCO, where the envelop error is restricted in a quarter of the range resolution cell and the phase error is limited no more than $\pi/4$ [1]. Even if the envelop is captured in a single range resolution bin, the residual phase error may severely degrade the quality of a SAR image in terms of geometric resolution, radiometric accuracy and irregular sidelobes. Hence, a more precise phase compensation procedure is as well indispensable in many SAR applications.

4 WCEA algorithm

For images corresponding to narrow swath, the phase errors caused by deviations from the ideal trajectory are almost the same for each range bin. However, large images with a number of range bins are liable to violate this assumption that the phase errors do not vary with range. We describe a weighted scheme to estimate the range-dependent residual phase errors and integrate them into PFA. The WCEA algorithm is simple to implement and substantially promotes the focus performance.

4.1 Phase error correction model

Combined with Fig. 1, the flight profile of the SAR platform at t_a is illustrated in Fig. 3, where P is the ideal position of the APC while A is its actual position with deviations of $\Delta y(t_a)$ in the Y-axis and $\Delta z(t_a)$ in the Z-axis. Clearly, the normal plane GPT_2 is perpendicular to the X-axis. T_3 is a target on the extension line of GT_2 and located in the mth ($m = 0, 1, …, M − 1$) range bin of the radar echo with $|T_3P| = R_m$, $|T_3A| = R_a(t_a)$ as well as the incident angle $\angle GPT_3 = \alpha_m$, where M is the number of samples in the range dimension. Other parameters are the same as those in Fig. 1. Herein, we suppose that the number of radar echoes is N and during the whole processing time, we denote the deviations of APC from the ideal path in the Y-axis and Z-axis as $\Delta y = \begin{bmatrix} \Delta y(0) & \Delta y(1) & \cdots & \Delta y(N-1) \end{bmatrix}$ and $\Delta z = \begin{bmatrix} \Delta z(0) & \Delta z(1) & \cdots & \Delta z(N-1) \end{bmatrix}$, respectively. For the nth ($n = 0, 1, …, N − 1$) radar echo, the slant range error of T_3 is $\Delta R_m(n) = R_a(n) - R_m$. However, in the traditional MOCO procedure, the error component that is perpendicular to PT_3 is insignificant and generally ignored. Consequently, the deviation PA can be decomposed into two parts: PD is considered as the range error affecting the focusing procedure and the insignificant component DA, vertical to PT_3, is neglected. Thus, the estimated
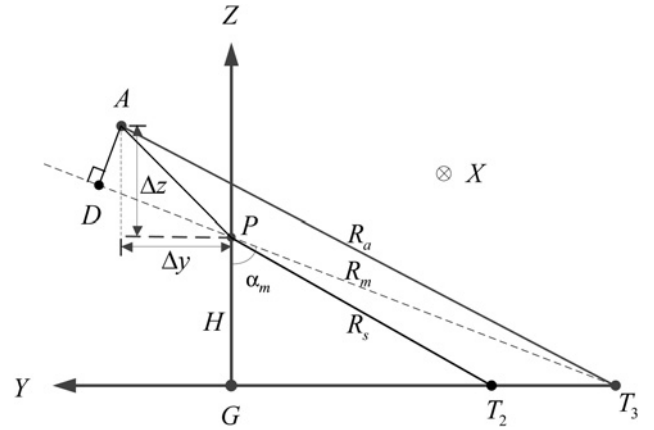

Fig. 3 *Flight profile of the SAR platform*

phase error can be written as

$$\vartheta_m(n) = \frac{4\pi}{\lambda} \times \Delta R_m(n) \simeq \frac{4\pi}{\lambda} \big(\Delta y(n) \sin \alpha_m + \Delta z(n) \cos \alpha_m \big) \quad (17)$$

Considering the spatial variance of the phase error and rewriting (17) using the matrix notation, we have

$$\boldsymbol{\Phi} = \boldsymbol{K}\boldsymbol{D}_1 \quad (18)$$

where

$$\boldsymbol{\Phi} = \begin{bmatrix} \boldsymbol{\Phi}(0, :) \\ \boldsymbol{\Phi}(1, :) \\ \vdots \\ \boldsymbol{\Phi}(M-1, :) \end{bmatrix}$$

is the estimated phase error matrix and $\boldsymbol{\Phi}(m, :) = \begin{bmatrix} \vartheta_m(0) & \vartheta_m(1) & \cdots & \vartheta_m(N-1) \end{bmatrix}$ demonstrates the phase error of mth range bin

$$\boldsymbol{K} = \frac{4\pi}{\lambda} \begin{bmatrix} \sin \alpha_0 & \sin \alpha_1 & \cdots & \sin \alpha_{M-1} \\ \cos \alpha_0 & \cos \alpha_1 & \cdots & \cos \alpha_{M-1} \end{bmatrix}^{\mathrm{T}}$$

is the parameter matrix and the superscript 'T' denotes the transpose

$$\boldsymbol{D}_1 = \begin{bmatrix} \Delta y \\ \Delta z \end{bmatrix}$$

represents the deviation matrix of the APC. However, in fact, the true range error of T_3 equals the difference of $R_a(n)$ and R_m, thus, the true phase error can be represented as

$$\vartheta_m^r(n) = \frac{4\pi}{\lambda} \big(R_a(n) - R_m \big) \quad (19)$$

where $R_a(n)$ can be expressed as $R_a(n) = \sqrt{\left(\sqrt{R_m^2 - H^2} + \Delta y(n) \right)^2 + (H + \Delta z(n))^2}$. Similarly, the true phase error matrix is given by

$$\boldsymbol{\Phi}^r = \begin{bmatrix} \boldsymbol{\Phi}^r(0, :) \\ \boldsymbol{\Phi}^r(1, :) \\ \vdots \\ \boldsymbol{\Phi}^r(M-1, :) \end{bmatrix}$$

with $\mathbf{\Phi^r}(m, :) = \begin{bmatrix} \vartheta_m^r(0) & \vartheta_m^r(1) & \cdots & \vartheta_m^r(N-1) \end{bmatrix}$. Obviously, the more $\mathbf{\Phi}$ approaches to $\mathbf{\Phi^r}$, the higher precise MOCO can be achieved. Meanwhile, taking the effects of the spatial variance of the phase error into account, we adopt a weighted scheme to estimate the range-dependent phase error, which will be discussed later.

4.2 Weighted autofocus scheme and phase error compensation

Autofocus is usually applied under the assumption that the RCM has been completely corrected. It begins with the range-compressed phase history domain, in which the data are compressed in range but not compressed in azimuth.

Suppose that the formation of a complex SAR image $f(m, k)$ is the focusing operation

$$f(m, k) = \frac{1}{N} \sum_{n=0}^{N-1} u(m, n) \exp\left(j\frac{2\pi nk}{N}\right) \qquad (20)$$

where $u(m, n)$ represents the phase history data after phase error correction and $k = 0, 1, \ldots, N-1$ refers to the index of azimuth positions within the focused image.

Let us construct a model associated with phase error corrupted data $u_0(m, n)$ in the phase history domain as

$$u(m, n) = u_0(m, n) \exp\left(j\vartheta_m^c(n)\right) \qquad (21)$$

where $\vartheta_m^c(n)$ is the phase correction component that cancels out the residual phase error in $u_0(m, n)$.

In addition, we use a well-known metric to measure the quality of a focused image, the contrast of a SAR image, which is defined as the ratio of the standard deviation of pixel magnitudes to the mean of pixel magnitudes and given by

$$C = \frac{1}{M} \sum_{m=0}^{M-1} \frac{\sigma_m}{\mu_m} \qquad (22)$$

where $\mu_m = (1/N) \sum_{k=0}^{N-1} |f(m, k)|$ and $\sigma_m = \sqrt{(1/N) \sum_{k=0}^{N-1} (|f(m, k)| - \mu_m)^2}$ [16, 17]. The image contrast can be considered as a measurement of the degree of the focus image because the contrast allows one to emphasise the difference in the amplitude of the scene. A high contrast measure is indicative of a sharp image, whereas a low contrast signifies that the image is out of focus. Also, the contrast is virtually independent of scene content and takes no statistical information of the isolated scatterers into account. It only requires the presence of contrast in the imaged area and does not require bright point targets, which can be easily satisfied in most situations.

We present here an autofocus approach for residual phase errors, that is, estimation and compensation of motion deviations that cause mainly undesirable phase undulations. The image contrast is utilised to reasonably measure the focusing quality of an SAR image. The more focused the image, the greater its contrast. To obtain the more focused image, the more accurate deviations of the APC must be estimated. Therefore, the phase error extraction problem is transformed to estimate the motion error of the APC to maximise the image contrast, which can be expressed as

$$\widehat{\mathbf{\Phi^c}} = \arg\max_{\mathbf{\Phi^c}}\left[C(\mathbf{\Phi^c})\right] \qquad (23)$$

where

$$\mathbf{\Phi^c} = \begin{bmatrix} \mathbf{\Phi^c}(0, :) \\ \mathbf{\Phi^c}(1, :) \\ \vdots \\ \mathbf{\Phi^c}(M-1, :) \end{bmatrix}$$

is the phase error correction matrix and $\mathbf{\Phi^c}(m, :) = \begin{bmatrix} \vartheta_m^c(0) \\ \vartheta_m^c(1) \cdots \vartheta_m^c(N-1) \end{bmatrix}$ denotes the phase error compensation component of mth range bin. Hence, (23) defines an unconstrained optimisation problem. Since there is no closed-form solution for $\mathbf{\Phi^c}$ that maximises C in (23), we find that an efficient and powerful way for solving this problem is to use conjugate gradient algorithm, which works well in solving a large-scale non-linear optimisation and conserves memory. The search, which is based on the gradient-based and iterative-based optimisation algorithm, finds coordinates of the maximum contrast measure. The estimation of the phase error deviating from the true kinematic parameters yields blurred images, while good estimates produce focused images. Using this method requires the explicit formulas for the gradient of C with respect to the phase correction vector $\vartheta_m^c(k)$, which can be shown as [16]

$$\frac{\mathrm{d}C}{\mathrm{d}\vartheta_m^c(n)} = \sum_{m=0}^{M-1} \gamma_m \mathrm{Im}\left[u^*(m, n)q(n)\right] \qquad (24)$$

where $\gamma_m = (-1/MN)\left((1/\sigma_m) + (\sigma_m/\mu_m^2)\right)$ and $q(n) = \sum_{k=0}^{N-1} \left(f(m, k)/|f(m, k)|\right) \exp\left(-j(2\pi kn/N)\right)$. In (24), we should note that the phase correction for each pulse in the azimuth dispersed data is considered as an independent variable, with the assumption that the phase error is identical for all range bins. For the sake of substantially reducing the computational burden for the phase error, a subset with high contrast of the available data is chosen to reconstruct a SAR image, while maintains the results of expected quality at the same time.

However, images with a large number of range bins begin to violate the assumption implied in (24) that the phase error does not vary with range. Hence, we adopt a weighted mean square error (WMSE) phase estimator in which the weights are determined by the contrasts of data in corresponding range bins. This phase estimation is more accurate than phase adjustment by contrast enhancement (PACE) illustrated in [17] because it does account for range varying behaviour of the phase error, while improves the accuracy of the estimate values by adjusting the weights of data in different range resolution cells. Moreover, with the contrast metric, this scheme is essentially more robust in the scene with no strong scatterers than other autofocus algorithms such as PGA.

To perform the described estimation, we establish a WMSE phase estimator as

$$\mathrm{WMSE}\left(\Delta y(n), \Delta z(n)\right) = \sum_{m=0}^{M-1} w_m \left(\vartheta_m(n) - \vartheta_m^r(n)\right)^2 \qquad (25)$$

where $C_m = \sigma_m/\mu_m$ ($m = 0, 1, \ldots, M-1$) is the contrast of data in the mth range bin; w_m is the corresponding weight and can be expressed as $w_m = C_m/\sum_{m=0}^{M-1} C_m$. Since the range bins with high contrast tend to have more features sensitive to variations in the phase error, the purpose of this optional weight w_m is to put more emphasis on the contribution of high contrast scenes than on that of the low ones to the estimation process of the induced phase error. Therefore, the weighting improves the overall accuracy of the estimation process.

By exploiting the WMSE estimator, we have

$$\frac{4\pi}{\lambda}\Delta y(n)\sum_{m=0}^{M-1}w_m\left(\sin\alpha_m\right)^2 + \frac{4\pi}{\lambda}\Delta z(n)\sum_{m=0}^{M-1}w_m\sin\alpha_m\cos\alpha_m$$
$$= \sum_{m=0}^{M-1}w_m\vartheta_m^r(n)\sin\alpha_m \qquad (26)$$

$$\frac{4\pi}{\lambda}\Delta y(n)\sum_{m=0}^{M-1}w_m\sin\alpha_m\cos\alpha_m + \frac{4\pi}{\lambda}\Delta z(n)\sum_{m=0}^{M-1}w_m\left(\cos\alpha_m\right)^2$$
$$= \sum_{m=0}^{M-1}w_m\vartheta_m^r(n)\cos\alpha_m \qquad (27)$$

The solutions to (26) and (27) give the expressions of $\Delta y(n)$ and $\Delta z(n)$.

However, only using the data of a single range bin to estimate the phase error is not reliable or robust in practical applications, in which clutters and noises may have a serious effect on the estimation. Moreover, this method results in an intensive computational burden at the same time. The division of the data set into narrow range sub-swaths can effectively solve this problem and is carried out in the phase history domain where the data is range compressed and azimuth non-compressed.

First, we break a large data set into V smaller sub-blocks in the range dimension with $M_1 = M/V$ range resolution cells in each sub-block so that the phase error of the data within each sub-block is approximately invariant along the range dimension. Then, PACE is used to average over many range bins to improve algorithm performance in terms of error-estimation accuracy, instead of utilising the data within a single range cell which is liable to be affected by strong clutters and noises. Here, we suppose that the distance $R(v)$ ($v = 0, 1, \ldots, V-1$) from the SAR ideal trajectory to the centre of the vth range sub-block is considered to be the reference range in the spatially variant phase correction procedure. Hence, the range error of the vth range sub-block is calculated and the analogous procedure applies to the next range sub-block. Finally, the phase errors are compensated by (26) and (27) in SAR data for excellent results. To further reduce the computational burden, we can select part of the range bins in each sub-block to estimate the phase errors.

From an overall perspective, a new 2D autofocus algorithm has been developed that estimates the RCM as well as the phase disturbing and proceeds envelop error compensation and phase error correction to properly focus the image. Apart from the image content with strong scatterers, our proposed algorithm is also robust and powerful for homogeneous areas in real-world SAR imaging. Additionally, when dealing with the range-variant phase errors, accurate phase error estimation is retrieved by means of WMSE estimator which is optimal in the sense that it has the weighted minimum mean square of the estimated errors. Finally, the whole processing is illustrated in Fig. 4 in detail. For PFA which relies on the unrealistic assumption of strictly planar wavefront propagation, the effects of the residual phase errors manifest themselves as spatially variant distortion and defocus in the image, which generally increases with distance from the scene centre [18, 19]. We can make some modifications proposed in [19] to allow a considerable increase in the focused scene diameter by a post-processing filtering technique for compensating the spatially variant blurring. Moreover, the along-track motion error is easy to be compensated by echo resampling in along-track direction and is not mentioned in this paper.

5 Real data experiments

Some real data experiments are conducted to demonstrate the validity of the proposed autofocus algorithm.

5.1 Real data processing

In the following, we give the results about real measured radar data processing to verify the feasibility of both envelop error correction and weighted scheme for phase error retrieval.

5.1.1 Scene with homogeneous areas: In this experiment, the data set is acquired by an X-band SAR working in the spotlight mode. The velocity of the platform is about 120 m/s with the pulse repeat frequency (PRF) 1250 Hz and the sampling rate
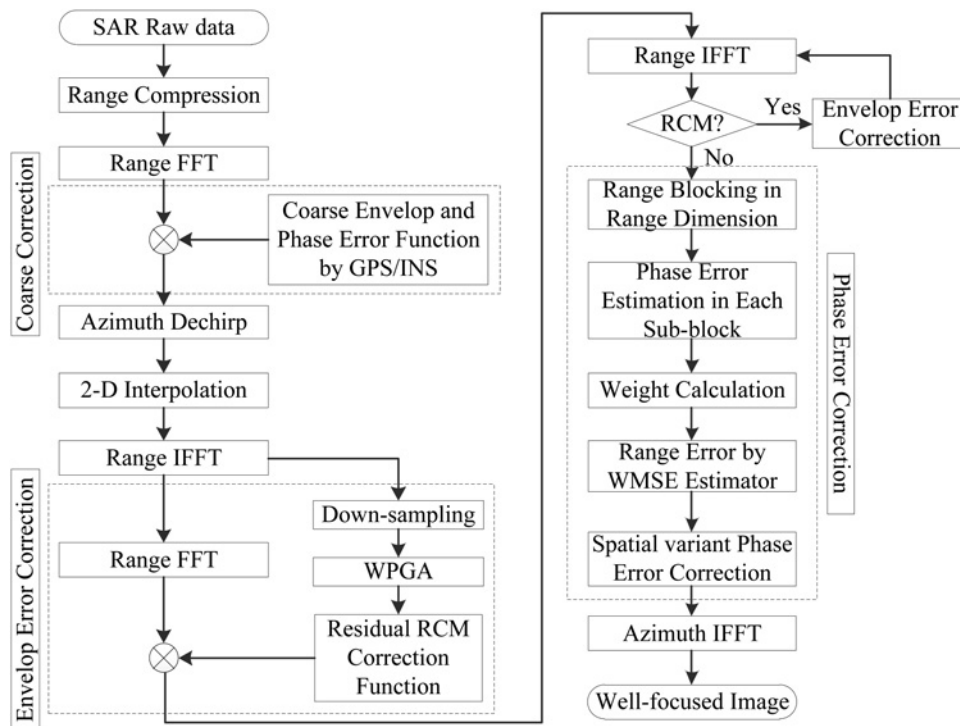

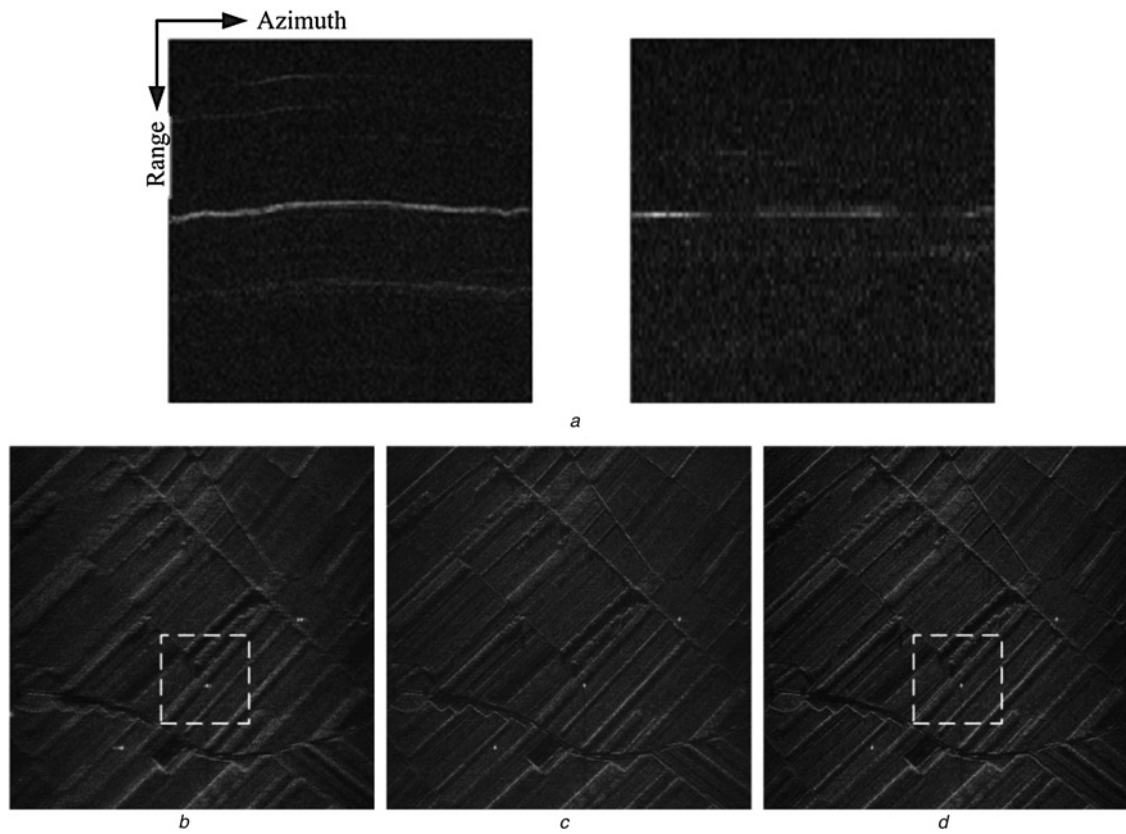**Fig. 4** *Flowchart of the proposed algorithm*

Fig. 5 *Processed results*

a Envelop with only GPS/INS information (left) and the proposed algorithm (right)
b SAR image without envelop error correction but with PACE for phase error correction
c SAR image with the proposed envelop error correction method and PACE for phase error correction
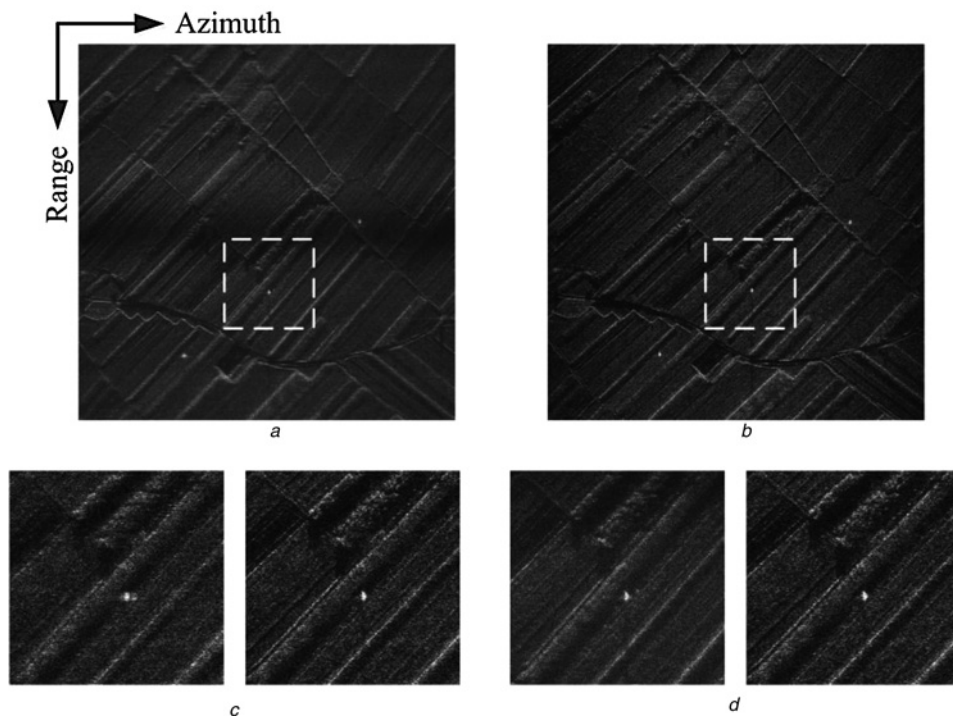*d* SAR image with the proposed algorithm

Fig. 6 *Processed SAR images*

a With CMD combined with the proposed envelop error correction method
b With ME-MOCO
c Magnified local images from the dotted frames in Fig. 5*b* (left) and Fig. 5*d* (right)
d Magnified local images from the dotted frames in Figs. *a* (left) and *b* (right)

Table 1 Image quality metrics

Figure	5b	5c	5d	6a	6b
entropy	16.2832	16.0487	15.8062	16.0624	15.8587
contrast	0.5223	0.5660	0.7172	0.5658	0.6829

Table 2 Radar parameters

Parameters	Values	Units
centre frequency	9.6	GHz
bandwidth	600	MHz
sampling rate	800	MHz
approximate platform velocity	105	m/s
reference slant range	15	km
PRF	1250	Hz

800 MHz. The height of the carrier is about 6.8 km and the reference slant range is 40.8 km. The accuracy of the navigation system is poor. What is more, the imaging scenario mainly consists of farmlands, grasslands and trees without strong scatterers, which can be seen as homogeneous areas.

To correct the envelop error, GPS/INS information is first utilised to coarsely remove part of the envelop error as well as the phase error, and then WPGA is employed to further remove the residual RCM on the range-compressed signal after the 2D polar formatting rather than the raw data. Figs. 5a and b shows the signal profiles by compensation with only GPS/INS information and by correction with the proposed envelop error correction method, respectively. Due to the effect of motion error, the signal envelop is not a straight line but a curve in the left of Fig. 5a. The vertical direction in figures is the range dimension, and the horizontal direction is the azimuth direction. Clearly, RCM is better compensated on the right of Fig. 5a, which indicates that the accuracy of the envelop error correction is beyond the capacity of the navigation system. The range profiles are just in a straight line after the proposed envelop error correction method and this testifies the performance of the described method.

In Fig. 5b, the SAR image is generated by PACE but without envelop error correction. The residual motion errors are still significant enough to cause serious blurring. Fig. 5c illustrates the SAR image with the proposed envelop error correction method and PACE for range-independent phase error correction, while Fig. 5d describes the result using the proposed algorithm, providing better focused region as well as more clearer texture about farmlands and grasslands in the imaged area. This certifies the necessity of the weighted scheme to compensate for the spatially variant phase errors and the better performance of the developed autofocus algorithm. Results in Figs. 6a and b are achieved by coherent MD (CMD) technique [20, 21] for phase error compensation (combined with the proposed envelop error correction method) and the minimum entropy MOCO (ME-MOCO) algorithm [12]. The entropies and contrasts of the SAR images obtained by different methods are listed in Table 1. The more focused the image, the smaller its entropy and the greater its contrast. Not only the weighted scheme gives better performance, but also the improvement is more pronounced.

For comparison, the magnified local images from the dotted frames within Figs. 5b, d and 6a, b are shown in Figs. 6c and d from left to right. Obviously, the image generated by the proposed algorithm can obtain the best results. Furthermore, the time consumed by removing phase errors in Figs. 5d and 6a, b are, respectively, 169.14, 177.48 and 240.65 s, which demonstrates that the described approach can surpass the recently proposed algorithms in processing speed but with better focusing performance. Therefore, the provided example demonstrates the advantages of the proposed algorithm, its capacity to handle the envelop error shifting through several range resolution cells in high-resolution SAR imaging and range-dependent phase errors in homogeneous scenarios.

5.1.2 Scene with strong scatterers: To demonstrate the performance of the proposed algorithm to deal with scenes with strong scatterers, we present the results of LML-WPGA [2] and the novel scheme. The parameters are shown in Table 2.

The final images focused on the slant plane are given in Figs. 7a and d by LML-WPGA and the presented autofocus algorithm, whose
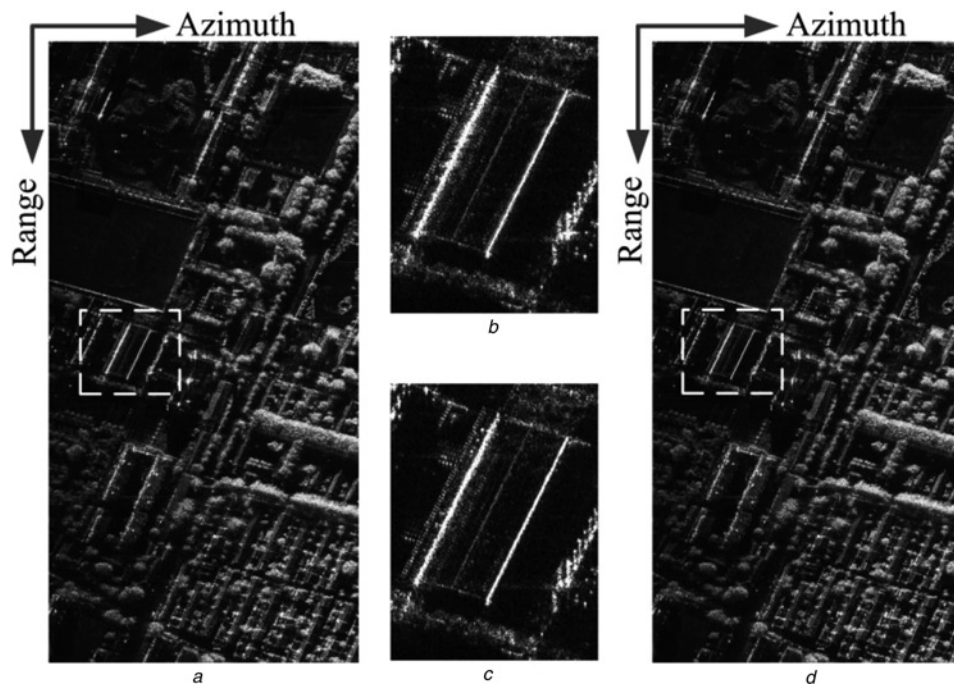
Fig. 7 *Processed SAR images*
a With LML-WPGA
b Magnified local image from the dotted frame in (a)
c Magnified local image from the dotted frame in (d)
d With the proposed algorithm

contrasts are 1.6914 and 1.6920, respectively. The horizontal direction is the azimuth dimension and the vertical direction is the range dimension. This experiment indicates that the performances of the images are well focused by both algorithms. The higher the contrast, the more focused the image. For further comparisons, Figs. 7b and 7c illustrate the magnified fragments of the scene correspondingly taken from Figs. 7a and d. The man-made metal points can be distinguished clearly, which validates the higher accuracy of the weighted scheme to compensate for the spatially variant phase errors and the better performance of the described autofocus algorithm. Therefore, the presented algorithm can also emulate the LML-WPGA in scenes with strong scatterers.

In summary, the proposed version of weighted scheme produces results with a reasonable amount of computations, while maintains high quality at the same time.

5.2 Future works

It was found that the proposed autofocus algorithm performed significantly well in both scenes with bright scatterers and homogenous areas. However, there are still some problems to be considered. First, the envelop error is inherently range variant, which can be prone to a departure from the assumption that the envelop error does not vary with range in some cases. Second, the strip-map mode is also widely used in the SAR applications. The proposed method for strip-map SAR should be further studied. In the future, the authors are going to examine these problems for a promoted estimation.

6 Conclusion

In this paper, a powerful and efficient autofocus algorithm for high-resolution spotlight SAR imaging integrated with PFA is presented. In high-resolution SAR imaging situation, RCM is more serious and may cause image distortion if not properly compensated. A coarse to fine idea is adopted to compensate for the envelop error exceeding more than one range resolution cell. First, a coarse correction of the envelop error as well as the phase error is carried out by GPS/INS information. Then the SSA strategy is designed to retrieve the excessive envelop error. Furthermore, a weighted scheme by WMSE estimator to compensate for range-varying phase errors has shown the expected results. Regardless of the image content and strong isolated scatterers, this method is more robust in homogenous scenes. Real measured data are used to demonstrate the versatility of the detailed approach.

7 Acknowledgments

8 References

1 Li, Y.K., Liu, C., Wang, Y.F., et al.: 'A robust motion error estimation method based on raw data', IEEE Trans. Geosci. Remote Sens., 2012, 50, (7), pp. 2780–2790
2 Zhang, L., Qiao, Z.J., Xing, M.D., et al.: 'A robust motion compensation approach for UAV SAR imagery', IEEE Trans. Geosci. Remote Sens., 2012, 50, (8), pp. 3202–3218
3 Sjanic, Z.: 'Navigation and mapping for aerial vehicles based on inertial and imaging sensors', PhD thesis, Linköping University, 2013
4 Xu, G., Xing, M.D., Zhang, L., et al.: 'Robust autofocusing approach for highly squinted SAR imagery using the extended wavenumber algorithm', IEEE Trans. Geosci. Remote Sens., 2013, 51, (10), pp. 5031–5046
5 Zhang, L., Sheng, J.L., Xing, M.D., et al.: 'Wavenumber-domain autofocus for highly squinted UAV SAR Imagery', IEEE Sens. J., 2012, 12, (5), pp. 1574–1588
6 Bezvesilniy, O.O., Gorovyi, I.M., Vavriv, D.M.: 'Estimation of phase errors in SAR data by local-quadratic map-drift autofocus'. Proc. of Int. Radar Symp. IRS 2012, Warsaw, Poland, May 2012, pp. 376–381
7 Wahl, D.E., Eichel, P.H., Ghiglia, D.C., et al.: 'Phase gradient autofocus – a robust tool for high resolution phase correction', IEEE Trans. Aerosp. Electron. Syst., 1994, 30, (3), pp. 827–835
8 Zhu, D.Y., Jiang, R., Mao, X.H., et al.: 'Multi-subaperture PGA for SAR autofocusing', IEEE Trans. Aerosp. Electron. Syst., 2013, 49, (1), pp. 468–488
9 Li, J.C., Chen, J., Liu, W., et al.: 'A synthetic bandwidth method for high-resolution SAR based on PGA in the range dimension', Sensors, 2015, 15, pp. 15339–15362
10 Naething, R.M., West, R.D.: 'Analysis of SAR autofocus performance'. Proc. SPIE, 2013, 8714, (871414), pp. 1–12
11 Gao, Y., Yu, W.D., Liu, Y.B., et al.: 'Sharpness-based autofocusing for Stripmap SAR using an adaptive-order polynomial model', IEEE Geosci. Remote Sens. Lett., 2014, 11, (6), pp. 1086–1090
12 Yang, L., Xing, M.D., Zhang, L., et al.: 'Entropy-based motion error correction for high-resolution spotlight SAR imagery', IET Radar Sonar Navig., 2012, 6, (7), pp. 627–637
13 Yang, L., Xing, M.D., Wang, Y., et al.: 'Compensation for the NsRCM and phase error after polar format resampling for airborne spotlight SAR raw data of high resolution', IEEE Geosci. Remote Sens. Lett., 2013, 10, (1), pp. 165–169
14 Musgrove, C., Naething, R.: 'A method to evaluate residual phase error for polar formatted synthetic aperture radar systems'. Proc. SPIE, 2013, 8714, (871413), pp. 1–10
15 Ye, W., Yeo, T.S., Bao, Z.: 'Weighted least-squares estimation of phase errors for SAR/ISAR autofocus', IEEE Trans. Geosci. Remote Sens., 1999, 37, (5), pp. 2487–2494
16 Yang, J.G., Huang, X.T., Jin, T., et al.: 'An interpolated phase adjustment by contrast enhancement algorithm for SAR', IEEE Geosci. Remote Sens. Lett., 2011, 8, (2), pp. 211–215
17 Yang, J.G., Huang, X.T., Jin, T., et al.: 'Polynomial phase adjustment by contrast enhancement algorithm for SAR'. EuSAR'12, Nuremberg, Germany, April 2012, pp. 599–602
18 Linnehan, R., Yasuda, M., Doerry, A.: 'An efficient means to mitigate wavefront curvature effects in polar format processed SAR Imagery'. Proc. SPIE, 2012, 8361, (83611N), pp. 1–9
19 Mao, X.H., Zhu, D.Y., Zhu, Z.D.: 'Polar format algorithm wavefront curvature compensation under arbitrary radar flight path', IEEE Geosci. Remote Sens. Lett., 2012, 9, (3), pp. 526–530
20 Samczynski, P., Kulpa, K.S.: 'Coherent mapdrift technique', IEEE Trans. Geosci. Remote Sens., 2010, 48, (3), pp. 1505–1517
21 Samczynski, P.: 'Superconvergent velocity estimator for an autofocus coherent mapdrift technique', IEEE Geosci. Remote Sens. Lett., 2012, 9, (2), pp. 204–208